LANGMUIR

pubs.acs.org/Langmuir Article

Multi-Foulant-Resistant Material Design by Matching Coating-Fluid Optical Properties

Cigdem Toparli, Max Carlson, Minh A. Dinh, Bilge Yildiz, and Michael P. Short*

Cite This: *Langmuir* 2020, 36, 4776–4784 Read Online

ACCESS | Metrics & More | Article Recommendations | Supporting Information

ABSTRACT: The buildup of corrosion deposits, known as fouling, seriously hinders large-scale energy production. From nuclear power plants to geothermal reservoirs, fouling increases system pressure drops, impedes heat transfer, and accelerates corrosion, leading to derating and early failure. Here, we investigate the collodial interactions between multiple foulants and coated surfaces, with the aim of discovering principles for minimizing the adhesion of foulants to them. We hypothesize that matching the full refractive index spectrum of a coating to its surrounding fluid minimizes the adhesion of all foulants entrained within and that the Lifshitz theory is sufficient to predict which materials will be multi-foulant-resistant. First-principle calculations of Hamaker constants and refractive indices of six foulants on six coatings in water correlate well to direct measurements of adhesion by atomic force microscopy (AFM)-based force spectroscopy. Amorphous 2% fluorine-doped tin oxide, crystalline SiO_2, CaF_2, and Na_3AlF_6, which all nearly match the refractive index spectrum of water, successfully resisted adhesion of six diverse foulant materials in aqueous AFM measurements. The validation of this design principle may be expanded to design multi-fouling-resistant coatings for any system in which van der Waals forces are the dominant adhesion mechanism.

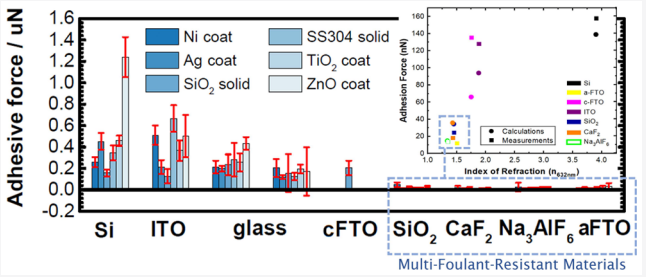

1. INTRODUCTION

Fouling is the unwanted accumulation of particles, microorganisms, macromolecules, and/or corrosion products on material surfaces.[1−3] Its buildup is one of the major issues plaguing geothermal heat extraction systems and nuclear power plants, among other systems, increasing operational costs and decreasing their economic viability[1,4−6] to the tune of 0.25% of the gross domestic product (GDP) of developed countries.[7] Fouling degrades systems that rely on fluid flow and heat transfer by increasing system pressure drops,[8] impeding heat transfer,[9] and accelerating corrosion by fostering oxidation[10] or concentrating chemical species within the foulant itself.[11] This leads directly to system derating[12] and early failure.[13] The situation is particularly dire in nuclear power plants, where the inability to control fouling results in less aggressive fuel loading patterns,[14] longer outages,[15] increased radiation dose to primary side workers,[16] mandatory power deratings,[17] and nuclear fuel failure by crud-induced localized corrosion (CILC).[18] To restore these functions, the deposits must be removed by techniques, such as ultrasonic cleaning[15] or manual removal,[8] or the affected part must be replaced.[4] However, these actions are often impractical, prolonging system outages and incurring significant costs as a result of downtime and component replacement. Therefore, it is crucial to prevent foulant deposition in the first place.

A number of studies have focused on developing technologies to inhibit fouling and corrosion in geothermal systems, for instance, scale inhibitors,[19] brine acidifiers,[20] steam cleaning,[21] polyphenylenesulfide-based or epoxy resin coatings,[22] or ceramic oxide coatings.[23] An important development in this field has been the design of polytetrafluoroethylene (PTFE, Teflon)-based coatings, which resist oxidation and scale buildup in briny water for 7 days at 200 °C.[4] However, none of these approaches is readily applicable in extreme environments, such as those found in geothermal and nuclear power plants.

Fouling is a process involving both thermodynamics and kinetics. The former determines whether fouling layers will grow at all, while the latter determines its rate once the first fouling layer deposits. In this work, we focus on the deposition of the initial foulant layer as the initiating event. The root of adhesion of foulant particles lies in their interactions with material surfaces, which can be comprised of many different types of surface forces.[24] In extreme environments of interest to large-scale energy production, where temperatures and pressures are too high to support electrochemical double

Received: December 25, 2019
Revised: April 2, 2020
Published: April 9, 2020

https://dx.doi.org/10.1021/acs.langmuir.9b03903
Langmuir 2020, 36, 4776–4784

layers,[25] this attraction is dominated by van der Waals (vdW) forces.[24,26] We also assume non-dominance of other forces, like magnetism, static charge, or steric bonding. In this scenario, minimizing vdW forces creates an atomistically slick surface, preventing foulant deposition. We test this hypothesis by a combination of density functional theory (DFT) and Hamaker calculations and liquid cell atomic force microscopy (AFM) colloidal probe measurements to determine the magnitude of the adhesion force between different foulants and coatings.

To calculate the vdW adhesion force, we use the Hamaker summation methodology,[26] a less complex expression of the full Lifshitz theory.[27] The Hamaker constant A_{Ham} describes the material and fluid-dependent vdW force magnitude.[28] We model the adhesion of a foulant particle to a coating surface using a sphere−plane geometry, with a spherical foulant and a planar coating, a reasonable approximation of particulate fouling on relatively smooth material surfaces. Assuming a sphere of radius R at a distance l from the plane and when $R \gg l$, the vdW adhesive force is given by

$$F_{\mathrm{vdW}} = \frac{A_{\mathrm{Ham}} R}{6l^2} \tag{1}$$

Minimizing A_{Ham} is therefore the key to slick, fouling-resistant surface design in large-scale energy systems. In this work, we use a full-spectrum Hamaker constant calculation,[29] minimizing the difference between the frequency-dependent refractive indices of water (our working fluid of choice) and potential coatings.[30] A_{Ham} is defined as the sum of all induced-dipole forces between two materials a and b interacting through an intervening fluid f.[24,31]

$$A_{\mathrm{Ham}} \approx \frac{3k_{\mathrm{B}}T}{2} \sum_{n=0}^{\infty} \Delta_{\mathrm{af}}(\xi_n)\Delta_{\mathrm{fb}}(\xi_n) R_n(l, \xi_n) \tag{2}$$

Here, k_{B} is Boltzmann's constant, T is the temperature in kelvin, R_n is an optical retardation factor described below, and $\Delta_{ij}(\xi_n)$ is the difference in material dielectric response at a particular imaginary frequency ξ_n

$$\Delta_{ij}(\xi) = \frac{\varepsilon_i(i\xi) - \varepsilon_j(i\xi)}{\varepsilon_i(i\xi) + \varepsilon_j(i\xi)} \tag{3}$$

where $\varepsilon_j(i\xi)$ is the dielectric function of material j evaluated at an imaginary frequency ξ for mathematical convenience,[32] resulting in a decaying function that allows for approximation of the infinite sum above with only a small number of its initial terms. To find $\varepsilon(i\xi)$ from a conventional real-frequency dielectric response $\varepsilon''(\omega)$, a Kramers−Kronig (KK) transform is used.

$$\varepsilon(i\xi) = 1 + \frac{2}{\pi}\int_0^{\infty} \frac{\omega\varepsilon''(\omega)}{\omega^2 + \xi^2} \tag{4}$$

The dielectric response is evaluated at discrete, imaginary frequencies ξ_n with

$$\xi_n = \frac{k_{\mathrm{B}}T}{h} n \tag{5}$$

where h is Planck's constant.

$R_n(l, \xi_n)$ are terms representing relativistic screening or retardation effects as a result of the finite time required for electromagnetic waves to travel across the fluid gap between the sphere and the plane. This is defined as[26]

$$R_n(l, \xi_n) = (1 + r_n)e^{-r_n}; \quad r_n = \frac{2ln_{\mathrm{f}}\xi_n}{c} \tag{6}$$

Here, n_{f} is the refractive index of the fluid evaluated at ξ_n, c is the speed of light, and the assumption is used that the refractive index of the coating is relatively similar to that of the fluid, which we ensure by our choice of materials. Because only the optical properties of the fluid and the sphere−plane spacing l affect the R_n terms, the impact of retardation screening is similar for all material pairs studied here. For $l = 1$ nm, chosen as an order of magnitude typical for interatomic spacing, the impact is a 0−1% decrease in force compared to the non-relativistic form (where R_n is taken to be unity). At a larger separation of l = 10 nm, there is a 10−20% decrease; therefore, this relativistic contribution should not be overlooked. This is particularly important when considering rougher surfaces, where considerable fluid may exist between the foulant and the material surface, despite some point contact.

Our design principle is based on a simplification of the above model, which was seen to apply well to our experimental measurements. The established Tabor−Winterton approximation (TWA)[33] provides an analytical expression for A_{Ham} that comes as a result of evaluating eq 2 using a single, visible-frequency oscillator model for $\varepsilon(\xi)$ of each material.

$$A_{\mathrm{Ham}} \approx \frac{3}{4}k_{\mathrm{B}}T\left(\frac{\varepsilon_{\mathrm{a}} - \varepsilon_{\mathrm{f}}}{\varepsilon_{\mathrm{a}} + \varepsilon_{\mathrm{f}}}\right)\left(\frac{\varepsilon_{\mathrm{b}} - \varepsilon_{\mathrm{f}}}{\varepsilon_{\mathrm{b}} + \varepsilon_{\mathrm{f}}}\right) + \frac{3\pi\hbar\nu_{\mathrm{e}}}{4\sqrt{2}} \frac{(n_{\mathrm{a}}^2 - n_{\mathrm{f}}^2)(n_{\mathrm{b}}^2 - n_{\mathrm{f}}^2)}{\sqrt{(n_{\mathrm{a}}^2 + n_{\mathrm{f}}^2)(n_{\mathrm{b}}^2 + n_{\mathrm{f}}^2)}\left(\sqrt{(n_{\mathrm{a}}^2 + n_{\mathrm{f}}^2)} + \sqrt{(n_{\mathrm{b}}^2 + n_{\mathrm{f}}^2)}\right)} \tag{7}$$

The first additive term accounts for electrostatic, dielectric polarizability, while the second term accounts for the oscillations of trapped electrons at one dominant (optical) frequency, assumed to comprise the plurality of induced-dipole interactions within the vdW force. Unlike the full-spectrum dependency of eq 2, in the TWA, only single and zero-frequency effects enter the equation. The decrease in mathematical richness of this approximation is countered by the simplicity of the design principle that can be derived from it. The above equation clarifies that minimizing $(n_{\mathrm{a}}^2 - n_{\mathrm{f}}^2)$ would result in a minimized Hamaker constant, regardless of n_{b}. This is the basis of our multi-fouling-resistant coating design principle.

We propose that choosing a material that has a refractive index close to that of its surrounding fluid will prevent foulant deposition, regardless of foulant type. The performance of this coating is expected to be even better if the full-spectral difference Δ_{af} can be made close to zero, by the same logic leading to multi-fouling-resistant behavior. The relationship between vdW forces and fouling deposition has been reported in the literature,[28,31] although it does not yet readily appear to have been experimentally exploited using our proposed design principle.

We investigate a series of low-refractive-index materials to show that anti-adhesion, multi-fouling-resistant coatings can be rapidly identified on the basis of the above TWA-based hypothesis and confirmed with full-spectral Hamaker calculations. We compare AFM measurements of the adhesion force to theoretical predictions and demonstrate that a combination of DFT and classical Hamaker calculations allows for accurate

https://dx.doi.org/10.1021/acs.langmuir.9b03903
Langmuir 2020, 36, 4776−4784

predictions of macroscopic fouling effects from atomistic unit cell calculations of optical properties.

2. MATERIALS AND METHODS

2.1. Summary of Methods Used. The interaction forces between each potentially multi-fouling-resistant coating, plus uncoated Si and glass substrates, and each of six types of foulant particles were measured using an AFM colloidal probe in a droplet of deionized water (>15 MΩ) to avoid ionic screening effects and to better match the water properties used in nuclear power plants. The roughness, chemistry, crystal phases, and refractive index spectra of the coatings were studied using AFM, X-ray photoelectron spectroscopy (XPS), grazing incidence X-ray diffraction (GIXD), and white light reflectometry, respectively, while coating thicknesses were obtained using focused ion beam (FIB) cross sectioning corroborated by white light reflectometry model fits. We used the Vienna Ab initio Simulation Package (VASP)[34] to perform first-principle calculations of the full-spectrum $\varepsilon''(\omega)$ of the same six candidate coatings, followed by a numerical solution of eqs 1 and 2 to obtain vdW forces (F_{vdW}), which are compared directly to AFM measurements.

2.2. Material Selection, Sourcing, and Characterization. Materials were chosen on the basis of their low-visible-range refractive indexes, alongside materials with relatively high refractive indices for clear comparison. Table 1 lists the materials investigated in this study

Table 1. Refractive Indices of Potentially Multi-Fouling-Resistant Materials Considered in This Study, Plus Examples of Passive Oxides Found in Nuclear and Geothermal Energy Systems

material	$n_{632\ nm}$	reference
H_2O	1.33	35
Si	3.9	35
crystalline FTO	2.01	37
amorphous FTO		
ITO	1.88	38 and 39
SiO_2	1.448	40 and 41
CaF_2	1.43	42 and 43
Na_3AlF_6	1.34	44 and 45
ZrO_2	2.15	46
Cr_2O_3	2.24	46
Fe_3O_4	2.34	47

and some common oxides naturally grown as passive layers in nuclear and geothermal energy systems (Cr_2O_3, Fe_3O_4, and ZrO_2) as high-n comparisons.

All fouling-resistant compounds were deposited onto Si wafers using physical vapor deposition (PVD) by PVD Products, Inc. on unheated substrates, with the exception of thin films of fluorine-doped tin oxide (FTO) and tin-doped indium oxide (ITO) purchased as coated glass slides from Sigma-Aldrich.

2.2.1. Crystal Structure Analysis. GIXD patterns were recorded to confirm the crystallographic phase of each as-deposted coating. These were obtained at grazing incidence ($\theta = 0.5°$) on a Rigaku SmartLab X-ray diffractometer through parallel-beam geometries operating at 45 kV and 200 mA. Full GIXD spectra for the as-deposited materials in this study can be found in the right half of Figure 2.

2.2.2. Surface Chemical Analysis. XPS (PHI VersaProbe III Scanning XPS Microprobe, Physical Electronics, Chanhassen, MN, U.S.A.) was performed to investigate the chemical composition of each material surface prior to atomic force microscopy-based force spectroscopy (AFM-FS) experiments, to confirm that the foulant-facing chemistry was as expected. Each sample was first sputtered with argon plasma for 10 min, to remove the surface oxide. A monochromatic Al Kα X-ray source (1486.6 eV) was operated at a pass energy of 187.85 eV, a step size of 0.1 eV over a measurement area of 10 × 10 μm, and a takeoff angle of 45°. Survey spectra were take from 100 to 1100 eV to identify the existence of different elements. High-resolution spectra of existing species were taken at a pass energy of 23.5 eV. The binding energy scale was referenced via a constant offset to the C−C signal at 284.8 eV. Quantitative analysis was carried out with CasaXPS 2.3.15 (http://www.casaxps.com/) to deconvolute any overlapping XPS peaks. Survey XPS spectra of all materials in this study can be found in Figure 1 of the Supporting Information, while detailed XPS spectra for the FTO variants are shown in Figure 2 of the Supporting Information.

2.2.3. Coating Thickness and Roughness Measurement. Cross-sectional analysis of each coating was performed after AFM-FS measurements using a gallium FIB (FEI Helios NanoLab 600 DualBeam system). A 1 μm thick Pt protective layer was deposited on the surfaces to prevent FIB damage to the coatings. To provide electrical conductivity for imaging, the SiO_2 sample was coated with ∼10 nm of gold. Images of the cross sections following FIB analysis are shown in Figure 3 of the Supporting Information. Coating surface roughnesses were also analyzed using AFM in scanning mode; these are shown on the left half of Figure 2.

2.3. Calculation and Measurement of vdW Forces. *2.3.1. Refractive Index Spectrum Measurement.* The refractive indices of the coatings were deduced from white light analysis (F20, Filmetrics, San Diego, CA, U.S.A.) working in the wavelength range of 190−1000 nm (6.5−1.2 eV) using a spot size of ∼7 mm. Background and reference spectra were taken on a Si-polished wafer. Data analysis was conducted using the FILMeasure software package (F20, Filmetrics, San Diego, CA, U.S.A.). n and k values from the literature were fitted using the measured coating thicknesses obtained from FIB cross-sectional analyses. Resulting refractive index spectra are shown in Figure 4 of the Supporting Information.

2.3.2. AFM Probe Preparation. Rectangular silicon nitride (Si_3N_4) lithographically fashioned TL-FM series cantilevers from Nanosensors were used in this study. For the functionalization of AFM-FS probes, 4 μm diameter microspheres were externally sourced from Cospheric, Inc. and confirmed in scanning electron microscopy (SEM) for correct diameter and sphericity. Spheres had to be at least 95% spherical to qualify for our tests, as defined by the minor and major axes of the normally elliptical geometry of any imperfect sphere. Figure 1 shows a SEM image of a 4 μm SiO_2 microsphere as affixed to

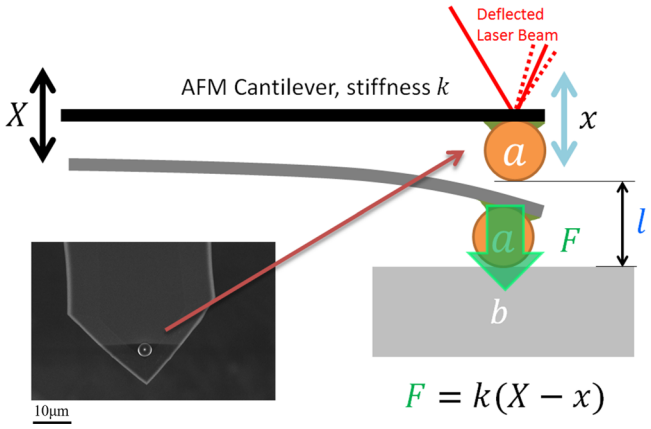

Figure 1. AFM-FS principle of operation and (inset) SEM image of a functionalized AFM-FS cantilever tip with a 4 μm SiO_2 microsphere.

one of our Si_3N_4 AFM-FS cantilevers. Attachment of the microspheres was carried out by Novascan, Inc., using a pick-and-place nanomanipulator to position the microsphere at the tip of the cantilever and a thermal adhesive to affix it. The foulant microspheres used in this work [Ni, Ag, SiO_2, TiO_2, 304 stainless steel (SS304), and ZnO] were obtained from Cospheric, Inc.

2.3.3. AFM-FS Measurements. All AFM measurements were performed in force−distance (FD) ramp mode using a Nano-Magnetics, Inc. ezAFM AQUA. The AFM was inserted into a custom-built environmental chamber, including an argon-sputtering gun

https://dx.doi.org/10.1021/acs.langmuir.9b03903
Langmuir 2020, 36, 4776−4784

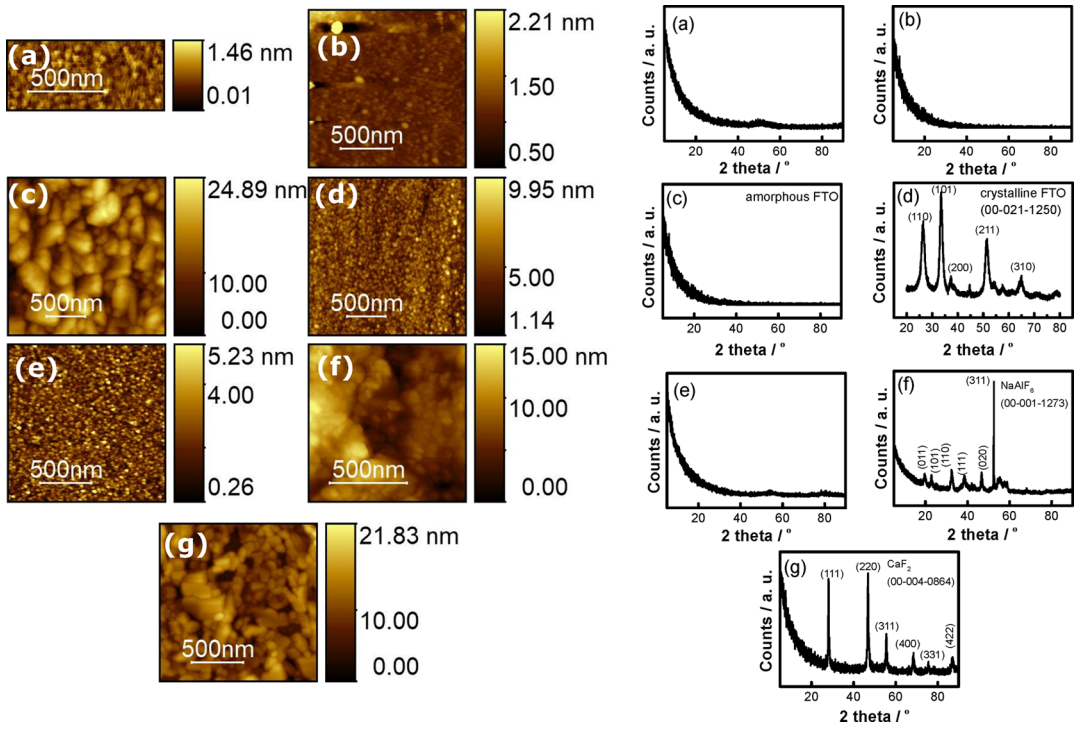

Figure 2. GIXD patterns (right) and surface roughnesses (left) of the coatings before contacting with water and foulants: (a) Si, (b) ITO, (c) a-FTO, (d) c-FTO, (e) SiO_2, (f) Na_3AlF_6, and (g) CaF_2.

system, used to pre-clean all coatings to avoid any spurious measurements of airborne contaminants. AFM-FS measurements were carried out by making contact between each representative foulant particle and coating pair. After contact was made, the cantilever was pulled away from the surface. The maximum downward force was kept constant at 100 nN by means of a deflection trigger mode. The adhesion measurements were carried out in a droplet of room temperature, deionized water (>15 MΩ). The probe was moved at a constant speed of 100 nm/s and to a total amplitude of 200 nm, with a sphere-surface contact time of approximately 100 ms per measurement. Measurements were performed on a point-by-point basis, with at least 10 μm separation between points, with measurement locations chosen at random to cover most of the 10 × 10 mm sample area. At least 50 points were measured on each sample.

Surface asperities, changes in roughness, thermal noise, and sample back-reflections of the laser beam contribute to uncertainty in the signal, resulting in large error bars. This is quite typical of AFM-FS measurements, where forces on the order of hundreds of piconewtons of signal must compete with all sources of electronic, optical, and vibrational noise. Measurements were conducted with multiple, randomized runs of each foulant-coating combination, with multiple, redundant tips and coatings to ensure that anomalies in any single material or method did not interfere with the data set.

2.3.4. Adhesive Force Calculation from AFM-FS Data. A ramp performed over a hard surface (here, a polished SiC sample) is used to determine the sensitivity S of the specific probe alignment and laser power. The piezo accuracy is verified by a tapping mode scan of a height calibration sample (HS series, Ted Pella, Inc.). A reference cantilever method,[48] with a Bruker CLFC series calibration probe, is used to determine the stiffness k of each of our probes. This method is chosen because its accuracy is unaffected by the presence of the microsphere on the test cantilever. Once the above calibrations are complete, the output of the quadrant photodiode ΔV in the pull-off section of a FD curve is converted to a force by eq 8.

$$F_{adh} = (\Delta V)Sk \tag{8}$$

2.3.5. First-Principle Calculation of Hamaker Constants. The adhesion of foulant-coating pairs in this work is also calculated using a combination of first-principle atomistic calculations on a unit cell scale to obtain optical properties and continuum Hamaker calculations to obtain a vdW force applied on a micrometer scale. This hybrid approach permits fast calculation times and, given its validity established in our study, permits the rapid computational evaluation of fouling-resistant materials that are less explored in the literature. The VASP DFT software[34] was used to find frequency-dependent dielectric response $\varepsilon''(\omega)$ for each studied material, using the optical functionality package within VASP.[49] This dielectric response is converted to $\varepsilon(i\xi)$ using eq 4. $\varepsilon(i\xi)$ of water is calculated using known optical properties.[50] Subsequently, the Hamaker constant for each foulant-coating pair is calculated using a finite series expansion of eq 2, with the limits given in eq 9.

$$A_{Ham} \approx \frac{3k_BT}{2}\sum_{n=0}^{1000}{}'\sum_{s=1}^{5}\frac{(\Delta_{af}\Delta_{fb}R)^s}{s^3} \tag{9}$$

Practically speaking, a unit cell of each material of interest was simulated in VASP. Each cell was constructed using literature values for lattice parameters. Following a geometric relaxation with atom position and cell volume optimization, the dielectric function is calculated using the LOPTICS flag. Projector augmented wave (PAW) Perdew–Burke–Ernzerhof (PBE) pseudo-potentials are used. A KPOINTS consistency check is performed for each material, with the number of K points satisfying $K > 50/a$, where a is the lattice spacing in angstroms. We use NEDOS = 2000 and NBANDS > $2N_o$, where N_o represents the bands resulting from the relaxation step.

2.4. Data Availability. All raw measurements, processing scripts, and VASP input files used in the creation of this manuscript are available at our permanent GitHub repository[51] for this study.

3. RESULTS AND DISCUSSION

In this work, we investigated four coatings predicted to be multi-foulant-resistant [SiO_2, amorphous FTO (a-FTO), CaF_2, and Na_3AlF_6] as well as materials with a range of refractive indices [ITO, pure Si, crystalline FTO (c-FTO), and

https://dx.doi.org/10.1021/acs.langmuir.9b03903
Langmuir 2020, 36, 4776−4784

borosilicate glass]. A range of metals (with and without passive oxide layers) and oxides (ranging from low to high refractive index) are used as colloidal probes, and most are commonly found foulants in nuclear and geothermal systems. These are Ni, Ag, SiO_2, SS304, TiO_2, and ZnO.

3.1. Characterization of As-Manufactured Coatings. Figure 2 shows the AFM-measured surface roughness and GIXD crystallographic characterization of representative areas of the coatings studied in this work.

GIXD results show that CaF_2 and Na_3AlF_6 are crystalline, while FTO made at room temperature, ITO, SiO_2, and bare Si are amorphous. FTO purchased from an outside supplier was measured by GIXD to be crystalline. The FTO samples are therefore referred to as a-FTO and c-FTO for amorphous and crystalline, respectively. The result for bare Si is incorrect, because the single-crystal Si wafer renders determination of the perfect three-dimensional (3D) angle difficult to catch the diffraction spot. Therefore, it is known that the bare Si wafer is crystalline, while all other GIXD results are representative of reality. XRD patterns of CaF_2 are consistent with the reported data in PDB file JPDC-00-004-0864, indicating a cubic crystalline structure. The XRD pattern of Na_3AlF_6 matches PDB file JPDC-00-001-1273, with a monoclinic structure. The diffraction from the Si substrate at 52° is clear on this material as well. More importantly, the FTO coating fabricated through PVD using substrate heating has a tetragonal structure matching SnO_2 as in PDB file JPDC-00-021-1250, while that manufactured with no substrate heating was amorphous.

Figure 2 also indicates that, initially, the surface roughness of the seven different coatings are comparable and relatively smooth. The root mean square (RMS) value of the coatings vary from 3 to 16 nm. Both RMS roughness values and contact angle measurements of each surface are summarized in Table 2. The surface roughness is used in translating AFM-measured surface forces to Hamaker constants, using the surface roughnesses as l in eqs 1, 2, and 6. Contact angle measurements were taken to ensure that contamination did not noticeably exist on surfaces by comparison to literature data. ITO and SiO_2 are confirmed to be hydrophobic, while Si, Na_3AlF_6, c-FTO, a-FTO, and CaF_2 are hydrophilic. The contact angle strongly depends upon surface preparation, which, in our case, is PVD deposition at room temperature.

Table 2. Contact Angle and RMS Surface Roughness Measurements of Coatings Tested in This Work

material	contact angle (deg)	surface roughness, RMS (nm)
Si	60.8 ± 5.0	0.273
c-FTO	77.2 ± 2.6	3.363
a-FTO	78.5 ± 2.2	14.874
ITO	105.5 ± 1.8	3.086
SiO_2	97.5 ± 2.0	0.512
CaF_2	40.1 ± 4.0	9.619
Na_3AlF_6	19.2 ± 1.52	15.528

3.2. AFM-FS Measurements of Coating-Foulant Adhesion in Water. Figure 3 shows the results of AFM-FS measurements between the six different foulants and six different coatings, plus uncoated Si and glass, recorded in a droplet of deionized water at 25 °C. Two major trends can be observed in the full data set in Figure 3a. First, uniformly 20–50× lower adhesion values of cryolite, fluorite, quartz, and amorphous FTO are observed, in comparison to uncoated samples. Second, in all materials with low refractive indices, the measured adhesive force is largely independent of the foulant, demonstrating the aforementioned "multi-foulant resistant" behavior. This is a key observation, because it suggests that no matter which foulant(s) will be encountered in an energy-producing system, these coatings or those similarly designed will resist fouling and deposition. Other notable observations include that uncoated Si exhibits the highest adhesive force and is definitively not multi-fouling-resistant.

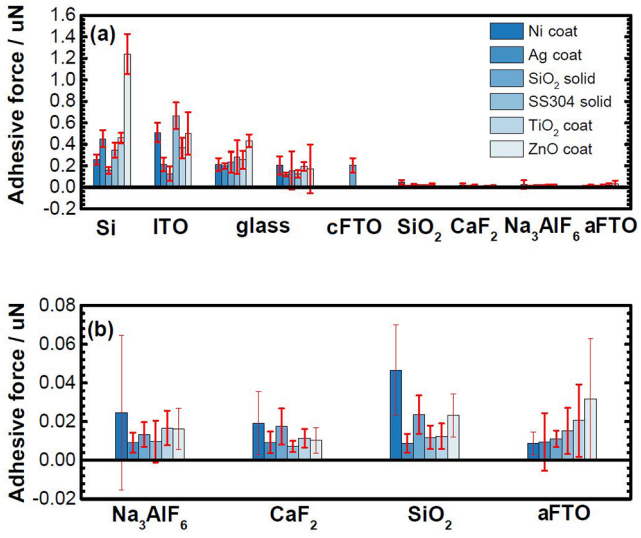

Figure 3. Direct AFM-FS meausurements of the coatings and foulants in a droplet of deionized water. The exemplary foulants in this work are Ni, Ag, SiO_2, SS304, TiO_2, and ZnO. (a) Full data set testing the multi-fouling-resistant nature of slick surfaces. "cFTO" is cyrstalline, while "aFTO" denotes the amorphous phase. (b) Coatings that exhibit the lowest adhesive force in panel a.

With only one exception (Ni on SiO_2), the slicker materials exhibited no statistically significant variation when testing the six different foulants. At the test conditions, passive oxides likely exist on the Ni and SS304 test spheres. However, these oxides are typically just a few nanometers thick, while VDW forces still act upon material thicknesses roughly 10 times this thickness. Sticky surfaces, because there is no match between refractive indices of the coating and the water, do not exhibit multi-fouling-resistant behavior nor should they, according to the TWA equation. This represents another key false-negative discrimination test, because the theory predicts that only slick surfaces will be multi-fouling-resistant and sticky materials will not. As a result of the requirement for keeping consistent measurement parameters (such as laser power and alignment) between multiple samples and probes and the need to cover large geometric areas on each sample, it was not feasible to attempt further error bar reduction. The various sources of error in this measurement are mainly statistical in nature, because the roughnesses of the as-deposited coatings are kept low as a result of their glass or Si wafer substrates and the size and spheroidicity of the functionalized SiO_2 microspheres coated with potential foulants were uniform. This renders a simple reporting of means and standard deviations to be a statistically accurate method of representing the data.

3.3. Analysis of Measured Refractive Indexes and Hamaker Constants. According to our hypothesis, the refractive index and the Hamaker constant are directly related to adhesion. It is expected on the basis of the literature

https://dx.doi.org/10.1021/acs.langmuir.9b03903
Langmuir 2020, 36, 4776–4784

Table 3. Empirical Fit of $\varepsilon(i\xi)$ for the Studied Materials as Found by DFT Simulation[a]

material	A (eV^2)	B (eV)	C (μL)	D (eV^2)	E (μL)	$A + D$ (eV^2)
Si	3.405	0.0007	0.0396	6.018	0.0718	9.423
ZrO_2	3.694	0.0175	0.017	0.5852	0.0017	4.2792
c-FTO	1.448	0.0629	0.012	1.862	0.0694	3.31
SiO_2	1.387	0.0151	0.0052	0.4307	9.546	1.8177
CaF_2	0.2318	0.0038	0.0015	0.6755	0.0099	0.9073
Na_3AlF_6	0.8325	0.0215	0.0032	0.8787	56.22	1.7112

[a]Parameters apply to eq 10.

Table 4. Materials Studied, FIB-Measured Coating Thicknesses, Experimental Measurement, and DFT Calculation of Refractive Indices of Potentially Multi-Fouling-Resistant Materials Considered in This Study and Their DFT-Calculated Hamaker Constants

material	d (nm)	experimental n_{632}	DFT n_{632}	literature n_{632}	reference	A_{Ham} (zJ)
Si	3000	3.86	4.418	3.9	35	24.07
c-FTO	300	2.18	1.98	2.01	37	17.87
a-FTO	900	1.41				
ITO	30	1.85	2.05	1.88	38 and 39	18.45
SiO_2	700	1.45	1.609	1.448	40 and 41	7.65
CaF_2	900	1.43	1.552	1.43	42 and 43	7.31
Na_3AlF_6	300	1.43	1.392	1.34	44 and 45	0.71

refractive indices that Na_3AlF_6 should exhibit the lowest adhesive force, while uncoated Si and glass should exhibit the highest adhesive forces. This conclusion holds true within the error bars of the data, both graphically in Figure 3 and numerically in Table 4. The AFM-FS measurements indicate that the room-temperature, PVD-manufactured FTO coating has the lowest average adhesive force, which was unexpected. It was determined by XRD (see Figure 2) that the FTO coating as formed by PVD is amorphous and not crystalline. A crystalline FTO sample (see Figure 2) was sourced for comparison and shows a higher adhesive force, as expected from its higher refractive index.

3.4. First-Principle Calculation of Hamaker Constants.

Using DFT, it was found empirically that a five-parameter expression based on a slightly altered formulation of ref 52, which removes the $1/\xi$ term for considerations of physicality,[53] provided an excellent fit ($R^2 \approx 0.999$) to $\varepsilon(i\xi)$ for all of the studied materials

$$\varepsilon(i\xi) \approx 1 + \frac{A}{1 + B\xi + C\xi^2} + \frac{D}{1 + E\xi^2} \quad (10)$$

where A–E are constants found by a least squares fit to the DFT dielectric function results of each material. These are summarized in Table 3 for the materials under study. Neglecting infrared (IR) oscillations for a coarse comparison, $A + D \propto n^2$, where n is the refractive index of the material,[53] and it is seen that the foulant-resistant materials have a lower $A + D$.

Table 4 compares the refractive indices found in this work and their published literature values. Most notable was the large difference between the experimental and published refractive index for what was found to be a-FTO compared to literature values for c-FTO, suggesting that the coating chemistry and/or structure did not match the sputtering target used to create it. This highlights the importance of the substrate temperature in forming a crystalline or amorphous film, because the XRD analyses confirm that an amorphous FTO film was grown from a crystalline FTO target. The DFT-calculated visible (632 nm) refractive indices of the materials under consideration in comparison to their adhesive forces is shown in Figure 4. Broad agreement in the trend between the

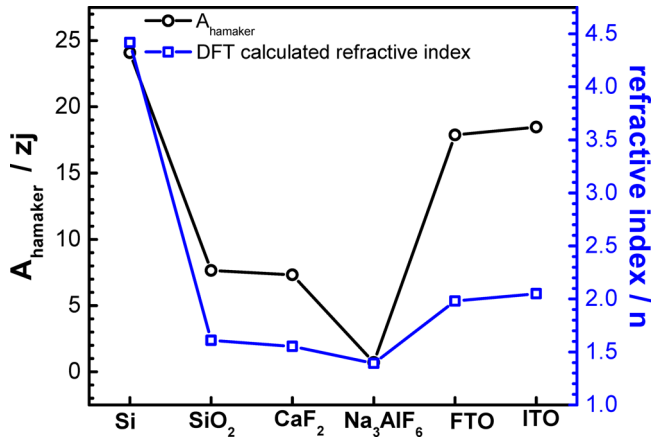

Figure 4. DFT-calculated Hamaker constants and refractive indices of potentially multi-fouling-resistant materials using crystalline SiO_2 as a foulant.

DFT-calculated refractive index and experimentally measured Hamaker constants helps to confirm our hypothesis that refractive indices can be used to choose or design multi-fouling-resistant coatings.

Optical data analysis and the full white light reflectometry spectra are given in the Supporting Information. It is clear that the adhesive force increases as the refractive index increases in the visible range. In contrast with the coatings, the refractive index of uncoated Si does not follow the adhesive force in the ultraviolet (UV) range, which confirms the TWA approximation.[33] It is also interesting to compare our obtained results to the literature. The refractive indices of Si, CaF_2, SiO_2, and ITO found in this work are consistent with the reported literature values.[38,41,42] The refractive index of the amorphous FTO initially grown in this study was found to be 1.41, while it is reported that crystalline FTO has a n of about 1.9.[36] In Figure 2, the GIXD pattern of FTO indicates that the FTO

https://dx.doi.org/10.1021/acs.langmuir.9b03903
Langmuir 2020, 36, 4776–4784

coating is amorphous, which could have significant impact on the refractive index. ITO used in this work was also found to be amorphous by GIXD; however, the n values of ITO obtained in this work and literature are consistent. The synthesis technique (PVD) and dopant amount would significantly affect the conductivity of FTO, and thus, changes in optical constants can be observed.

The reported refractive index for Na_3AlF_6 is 1.44, while our measured value from white light spectroscopy is 1.49. The Na_3AlF_6 coating is crystalline, as shown in Figure 2, although a Si substrate peak is also observed. The difference between literature data and our experimental data could originate from the inhomogeneity of the film. In this work, a smooth, bare Si wafer was used as a substrate for some potentially multi-fouling-resistant coating depositions and also measured in uncoated form to validate effectiveness of the coating layer. As expected, the uncoated wafer shows the highest adhesive force and also has the highest refractive index. However, the refractive index measured in this work, 3.86, is slightly lower than the literature value of 3.97.

As a final validation of our multi-fouling-resistant design principle, the DFT-calculated vdW forces and refractive indices of the coatings in this study are shown in Figure 5. Among all

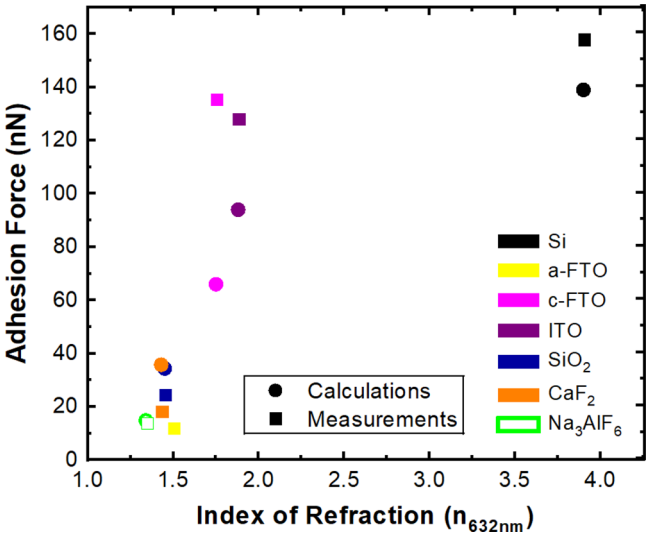

Figure 5. Comparison of measured SiO_2 foulant adhesive force on different coating materials and DFT−Hamaker-calculated adhesive force, as a function of visible refractive indices of Na_3AlF_6, CaF_2, SiO_2, Si, a-FTO, c-FTO, and ITO. Full-spectral refractive indices of coatings are shown in the Supporting Information.

surfaces tested, Si has the highest Hamaker constant and highest refractive index, while the Hamaker constant and refractive index of Na_3AlF_6 are the lowest. CaF_2 and SiO_2 have closer Hamaker constants and refractive indices. The Hamaker constant and refractive indices of FTO and ITO are higher than CaF_2 and SiO_2, although it should be noted that DFT was used to calculate Hamaker constants of only the crystalline phases of all materials. The results from the DFT calculation confirms our hypothesis that the lower refractive index coatings will exhibit lower adhesive forces to foulants.

4. CONCLUSION

We hypothesized and demonstrated a multi-foulant-resistant coating design principle, which assumes that vdW forces will dominate attractions between collodial particles and surfaces. We showed a strong, quantitative correlation between DFT-calculated and experimentally measured adhesion forces for the multi-foulant-resistant materials, demonstrating that, while VDW forces are not the only surface forces acting to initiate fouling, they are a strong predictor of antifouling coatings. Equally important is the proposed and demonstrated multi-foulant-resistant feature of this approach, shown here to be valid for both metallic and non-metallic foulants. Further improvements could be made by mixing two or more coating materials to best match the refractive spectrum of a working fluid. This design principle, when combined with additional, system-specific constraints (such as low neutron absorption cross section in nuclear power plants or H_2S corrosion resistance in geothermal systems), represents a useful tool to reduce or eliminate fouling as a scourge to large-scale, carbon-free energy production.

■ ASSOCIATED CONTENT

Supporting Information

The Supporting Information is available free of charge at https://pubs.acs.org/doi/10.1021/acs.langmuir.9b03903.

XPS survey spectra of potentially foulant-agnostic coatings: (a) Si substrate, (b) SiO_2, (c) CaF_2, (d) Na_3AlF_6, (e) ITO, (f) a-FTO, and (g) c-FTO (Figure 1), high-resolution scan of the F peak: (a) a-FTO and (b) c-FTO (Figure 2), cross-section images of the coatings obtained by FIB analysis: (a) CaF_2, (b) Na_3AlF_6, (c) a-FTO, (d) ITO, (e) SiO_2, and (f) c-FTO (Figure 3), and full spectral optical constants deduced from white light interferometry, with the thicknesses obtained from FIB cross-sectional analysis were used as input parameters: (a) CaF_2, (b) Na_3AlF_6, (c) a-FTO, (d) ITO, (e) SiO_2, (f) Si, and (g) c-FTO (Figure 4) (PDF)

■ AUTHOR INFORMATION

Corresponding Author

Michael P. Short − *Department of Nuclear Science and Engineering, Massachusetts Institute of Technology, Cambridge, Massachusetts 02139, United States;* orcid.org/0000-0002-9216-2482; Phone: +1-617-347-7763; Email: hereiam@mit.edu

Authors

Cigdem Toparli − *Department of Nuclear Science and Engineering, Massachusetts Institute of Technology, Cambridge, Massachusetts 02139, United States*

Max Carlson − *Department of Nuclear Science and Engineering, Massachusetts Institute of Technology, Cambridge, Massachusetts 02139, United States*

Minh A. Dinh − *Department of Nuclear Science and Engineering, Massachusetts Institute of Technology, Cambridge, Massachusetts 02139, United States*

Bilge Yildiz − *Department of Nuclear Science and Engineering and Department of Materials Science and Engineering, Massachusetts Institute of Technology, Cambridge, Massachusetts 02139, United States;* orcid.org/0000-0002-2688-5666

Complete contact information is available at: https://pubs.acs.org/10.1021/acs.langmuir.9b03903

https://dx.doi.org/10.1021/acs.langmuir.9b03903
Langmuir 2020, 36, 4776−4784

Notes

The authors declare no competing financial interest.

■ ACKNOWLEDGMENTS

The authors thank Prof. Robert Simpson of the Singapore University of Technology and Design (SUTD) for ideas on how to further improve these multi-foulant-resistant coatings. The authors gratefully acknowledge financial support from the Exelon Corporation through the MIT Energy Initiative (MITEI) Center for Advanced Nuclear Energy Systems (CANES), MITEI Low-Carbon Energy Center (LCEC), Statoil Petroleum AS (now Equinor) under MITEI Sustaining Member Agreement 4502981450, the CANES LCEC, and the International Collaborative Energy Technology (ICET) R&D Program (Grant 20168540000030) of the Korea Institute of Energy Technology Evaluation and Planning (KETEP), which is funded by the Korean Ministry of Trade Industry and Energy. This material is based on work supported by the National Science Foundation Graduate Research Fellowship under Grant 1122374. Any opinion, findings, and conclusions or recommendations expressed in this material are those of the authors and do not necessarily reflect the views of the National Science Foundation.

■ REFERENCES

(1) Chan, S. H. Fouling of Geothermal Energy Systems. In *Fouling Science and Technology*; Melo, L. F., Bott, T. R., Bernardo, C. A., Eds.; Springer: Dordrecht, Netherlands, 1988; NATO ASI Series (Series E: Applied Sciences), Vol. *145*, pp 649−667, DOI: 10.1007/978-94-009-2813-8_42.

(2) Tesler, A. B.; Kim, P.; Kolle, S.; Howell, C.; Ahanotu, O.; Aizenberg, J. Extremely durable biofouling-resistant metallic surfaces based on electrodeposited nanoporous tungstite films on steel. *Nat. Commun.* **2015**, *6*, 8649.

(3) de Messano, L. V. R.; Sathler, L.; Reznik, L. Y.; Coutinho, R. The effect of biofouling on localized corrosion of the stainless steels N08904 and UNS S32760. *Int. Biodeterior. Biodegrad.* **2009**, *63*, 607−614.

(4) Sugama, T.; Gawlik, K. Anti-silica fouling coatings in geothermal environments. *Mater. Lett.* **2002**, *57*, 666−673.

(5) Ning, C.; Mingyan, L.; Weidong, Z. Fouling and Corrosion Properties of SiO2 Coatings on Copper in Geothermal Water. *Ind. Eng. Chem. Res.* **2012**, *51*, 6001−6017.

(6) Gunnarsson, I.; Arnórsson, S. Impact of silica scaling on the efficiency of heat extraction from high-temperature geothermal fluids. *Geothermics* **2005**, *34*, 320−329.

(7) Müller-Steinhagen, H.; Malayeri, M. R.; Watkinson, A. P. Heat Exchanger Fouling and Cleaning—2011. *Heat Transfer Eng.* **2013**, *34*, 653−654.

(8) Deshon, J.; Hussey, D.; Kendrick, B. K.; McGurk, J.; Secker, J.; Short, M. P. Pressurized water reactor fuel crud and corrosion modeling. *JOM* **2011**, *63*, 64.

(9) Deshon, J.; Wang, G.; Byers, W. A.; Young, M. *Simulated Fuel Crud Thermal Conductivity Measurements under Pressurized Water Reactor Conditions*; Electric Power Research Institute (EPRI): Palo Alto, CA, 2011; Technical Report 1022896.

(10) Galoppi, G.; Biliotti, D.; Ferrara, G.; Carnevale, E. A.; Ferrari, L. Feasibility Study of a Geothermal Power Plant with a Double-pipe Heat Exchanger. *Energy Procedia* **2015**, *81*, 193−204.

(11) Henshaw, J.; McGurk, J. C.; Sims, H. E.; Tuson, A.; Dickinson, S.; Deshon, J. A model of chemistry and thermal hydraulics in PWR fuel crud deposits. *J. Nucl. Mater.* **2006**, *353*, 1−11.

(12) Uchida, S.; Asakura, Y.; Suzuki, H. Deposition of boron on fuel rod surface under sub-cooled boiling conditions—An approach toward understanding AOA occurrence. *Nucl. Eng. Des.* **2011**, *241*, 2398−2410.

(13) Allen, T.; Busby, J.; Meyer, M.; Petti, D. Materials challenges for nuclear systems. *Mater. Today* **2010**, *13*, 14−23.

(14) Lukic, Y. D.; Schmidt, J. S. Fuel assemblies in a reactor core and method of designing and arranging same. U.S. Patent 6,891,912, May 10, 2005.

(15) Kondoh, K.; Fujita, C.; Sakai, H.; Hirose, E. Crud removal for fuel assembly by ultrasonic cleaning. *Karyoku Genshiryoku Hatsuden* **1994**, *45*, 670−674.

(16) United States Nuclear Regulatory Commission (U.S. NRC). *Identification of Unresolved Safety Issues Relating to Nuclear Power Plants*; U.S. NRC: Washington, D.C., 1979; Report to Congress NUREG-0510.

(17) Frattini, P. L.; Varrin, R. D.; Hunt, E. S. Apparatus and method for ultrasonically cleaning irradiated nuclear fuel assemblies. U.S. Patent 6,396,892, May 28, 2002.

(18) Yang, R.; Cheng, B.; Deshon, J.; Edsinger, K.; Ozer, O. Fuel R & D to improve fuel reliability. *J. Nucl. Sci. Technol.* **2006**, *43*, 951−959.

(19) Rousseau, A. F.; Partridge, J. G.; Mayes, E. L. H.; Toton, J. T.; Kracica, M.; McCulloch, D. G.; Doyle, E. D. Microstructural and tribological characterisation of a nitriding/TiAlN PVD coating duplex treatment applied to M2 High Speed Steel tools. *Surf. Coat. Technol.* **2015**, *272*, 403−408.

(20) Mundhenk, N.; Huttenloch, P.; Sanjuan, B.; Kohl, T.; Steger, H.; Zorn, R. Corrosion and scaling as interrelated phenomena in an operating geothermal power plant. *Corros. Sci.* **2013**, *70*, 17−28.

(21) Gudipati, C. S.; Finlay, J. A.; Callow, J. A.; Callow, M. E.; Wooley, K. L. The Antifouling and Fouling-Release Perfomance of Hyperbranched Fluoropolymer (HBFP)Poly(ethylene glycol) (PEG) Composite Coatings Evaluated by Adsorption of Biomacromolecules and the Green Fouling Alga Ulva. *Langmuir* **2005**, *21*, 3044−3053.

(22) Zhang, F.; Liu, M. Y.; Zhou, W. D. Inhibition of fouling with titania and silica coatings on plate heat exchanger in 80 °C simulated geothermal water. *Heat Exchanger Fouling and Cleaning* **2017**, *8*, 183−190.

(23) Cai, Y.; Quan, X.; Li, G.; Gao, N. Anticorrosion and Scale Behaviors of Nanostructured ZrO_2TiO_2 Coatings in Simulated Geothermal Water. *Ind. Eng. Chem. Res.* **2016**, *55*, 11480−11494.

(24) Israelachvili, J. N. Van der Waals Forces. *Intermolecular and Surface Forces*, 3rd ed.; Academic Press: San Diego, CA, 2011; Chapter 6, pp 107−132, DOI: 10.1016/B978-0-12-391927-4.10006-4.

(25) Klapetek, P. *Quantitative Data Processing in Scanning Probe Microscopy: SPM Applications for Nanometrology*, 2nd ed.; Elsevier: Amsterdam, Netherlands, 2018; DOI: 10.1016/C2016-0-04404-2.

(26) Parsegian, V. A. *Van der Waals Forces: A Handbook for Biologists, Chemists, Engineers, and Physicists*; Cambridge University Press: Cambridge, U.K., 2005; DOI: 10.1017/CBO9780511614606.

(27) Lifshitz, E. M. The theory of molecular attractive forces between solids. *Sov. Phys. JETP* **1956**, *2*, 73−83.

(28) Oliveira, R. Understanding adhesion: A means for preventing fouling. *Exp. Therm. Fluid Sci.* **1997**, *14*, 316−322.

(29) Bergström, L.; Meurk, A.; Arwin, H.; Rowcliffe, D. J. Estimation of Hamaker Constants of Ceramic Materials from Optical Data Using Lifshitz Theory. *J. Am. Ceram. Soc.* **1996**, *79*, 339−348.

(30) Fronczak, S. G.; Browne, C. A.; Krenek, E. C.; Beaudoin, S. P.; Corti, D. S. Non-contact AFM measurement of the Hamaker constants of solids: Calibrating cantilever geometries. *J. Colloid Interface Sci.* **2018**, *517*, 213−220.

(31) Dumnernchanvanit, I.; Zhang, N. Q.; Robertson, S.; Delmore, A.; Carlson, M. B.; Hussey, D.; Short, M. P. Initial experimental evaluation of crud-resistant materials for light water reactors. *J. Nucl. Mater.* **2018**, *498*, 1−8.

(32) *Casimir Physics*; Dalvit, D., Milonni, P., Roberts, D., da Rosa, F., Eds.; Springer: Berlin, Germany, 2011; Lecture Notes in Physics, Vol. *834*, DOI: 10.1007/978-3-642-20288-9.

(33) French, R. H.; Cannon, R. M.; DeNoyer, L. K.; Chiang, Y. M. Full spectral calculation of non-retarded Hamaker constants for

https://dx.doi.org/10.1021/acs.langmuir.9b03903
Langmuir 2020, 36, 4776−4784

ceramic systems from interband transition strengths. *Solid State Ionics* **1995**, *75*, 13−33.
(34) Hafner, J. Ab-initio simulations of materials using VASP: Density-functional theory and beyond. *J. Comput. Chem.* **2008**, *29*, 2044−2078.
(35) Aspnes, D. E.; Studna, A. A. Dielectric functions and optical parameters of Si, Ge, GaP, GaAs, GaSb, InP, InAs, and InSb from 1.5 to 6.0 eV. *Phys. Rev. B: Condens. Matter Mater. Phys.* **1983**, *27*, 985−1009.
(36) Ball, J. M.; Stranks, S. D.; Hörantner, M. T.; Hüttner, S.; Zhang, W.; Crossland, E. J. W.; Ramirez, I.; Riede, M.; Johnston, M. B.; Friend, R. H.; Snaith, H. J. Optical properties and limiting photocurrent of thin-film perovskite solar cells. *Energy Environ. Sci.* **2015**, *8*, 602−609.
(37) Zahran, H. Y.; Iqbal, J.; Yahia, I. S. Optical constants and nonlinear calculations of fluorescein/FTO thin film optical system. *Phys. B* **2016**, *500*, 98−105.
(38) Moerland, R. J.; Hoogenboom, J. P. Subnanometer-accuracy optical distance ruler based on fluorescence quenching by transparent conductors. *Optica* **2016**, *3*, 112−117.
(39) Burrows, P. E.; Gu, G.; Forrest, S. R.; Vicenzi, E. P.; Zhou, T. X. Semitransparent cathodes for organic light emitting devices. *J. Appl. Phys.* **2000**, *87*, 3080−3085.
(40) Tan, C. Z. Determination of refractive index of silica glass for infrared wavelengths by IR spectroscopy. *J. Non-Cryst. Solids* **1998**, *223*, 158−163.
(41) Malitson, I. H. Interspecimen Comparison of the Refractive Index of Fused Silica. *J. Opt. Soc. Am.* **1965**, *55*, 1205−1209.
(42) Malitson, I. H. A Redetermination of Some Optical Properties of Calcium Fluoride. *Appl. Opt.* **1963**, *2*, 1103−1107.
(43) Daimon, M.; Masumura, A. High-accuracy measurements of the refractive index and its temperature coefficient of calcium fluoride in a wide wavelength range from 138 to 2326 nm. *Appl. Opt.* **2002**, *41*, 5275−5281.
(44) Netterfield, R. P. Refractive indices of zinc sulfide and cryolite in multilayer stacks. *Appl. Opt.* **1976**, *15*, 1969−1973.
(45) Heitmann, W. The influence of various parameters on the refractive index of evaporated dielectric films. *Appl. Opt.* **1968**, *7*, 1541−1544.
(46) Wood, D. L.; Nassau, K. Refractive index of cubic zirconia stabilized with yttria. *Appl. Opt.* **1982**, *21*, 2978−2981.
(47) Fang, X.; Xuan, Y.; Li, Q. Measurement of the extinction coefficients of magnetic fluids. *Nanoscale Res. Lett.* **2011**, *6*, 237.
(48) Torii, A.; Sasaki, M.; Hane, K.; Okuma, S. A method for determining the spring constant of cantilevers for atomic force microscopy. *Meas. Sci. Technol.* **1996**, *7*, 179−184.
(49) Gajdoš, M.; Hummer, K.; Kresse, G.; Furthmüller, J.; Bechstedt, F. Linear optical properties in the projector-augmented wave methodology. *Phys. Rev. B: Condens. Matter Mater. Phys.* **2006**, *73*, 045112.
(50) Harvey, A. H.; Gallagher, J. S.; Sengers, J. M. H. L. Revised Formulation for the Refractive Index of Water and Steam as a Function of Wavelength, Temperature and Density. *J. Phys. Chem. Ref. Data* **1998**, *27*, 761−774.
(51) *GitHub Data Repository*, 2019; https://github.com/shortlab/2018-FoulingAgnostic-Paper, DOI: 10.5281/zenodo.2593837.
(52) Bergström, L. Hamaker constants of inorganic materials. *Adv. Colloid Interface Sci.* **1997**, *70*, 125−169.
(53) Hough, D. B.; White, L. R. The calculation of hamaker constants from liftshitz theory with applications to wetting phenomena. *Adv. Colloid Interface Sci.* **1980**, *14*, 3−41.

https://dx.doi.org/10.1021/acs.langmuir.9b03903
Langmuir 2020, 36, 4776−4784